J. Fluid Mech. (2023), *vol*. 974, A40, doi:10.1017/jfm.2023.728

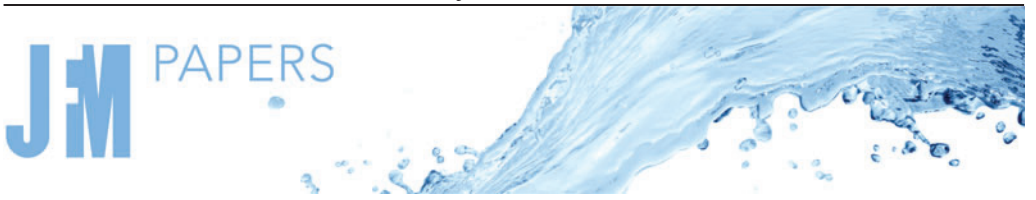

Direct numerical simulation of turbulent flow in pipes with realistic large roughness at the wall

Mariangela De Maio[1],†, **Beatrice Latini**[1], **Francesco Nasuti**[1] and **Sergio Pirozzoli**[1]

[1]Dipartimento di Ingegneria Meccanica e Aerospaziale, Sapienza Università di Roma, via Eudossiana 18, 00184 Roma, Italy

(Received 19 January 2023; revised 24 August 2023; accepted 30 August 2023)

We carry out direct numerical simulation (DNS) of turbulent flow in rough pipes. Two types of irregular roughness are investigated, namely a grit-blasted and a graphite surface. A wide range of Reynolds numbers is tested, from the laminar up to the fully rough regime, attempting to replicate Nikuradse's pioneering study. Despite the large relative roughness, outer-layer similarity is achieved at high Reynolds number as hypothesised by Townsend, with deviations from the smooth wall case of 4 % for the grit-blasted surface and 13 % for the graphite surface. This makes it possible to define a roughness function and the equivalent sand-grain roughness. The results are compared with those obtained in plane channels, with small differences pointing to the residual influence of the duct cross-sectional shape in the presence of relatively large roughness. The computed friction factors behave similar to those Nikuradse's chart, with differences in terms of the friction factor in the laminar region and of the critical Reynolds number, which are partly absorbed by using the hydraulic radius as reference length scale. The distributions of the velocity fluctuations intensities point to a isotropisation of turbulence in the near-wall region resulting from the roughness, with influence of the roughness geometry. Comparison of the computed equivalent sand-grain roughness height suggest that existing correlations suffer from poor predictive power, at least for surfaces with large relative roughness.

Key words: pipe flow

1. Introduction

Pressure-driven flow in ducts is a subject of utmost relevance in mechanical and aerospace engineering applications. In fact, effective design of ducts in cooling systems of liquid

† Email address for correspondence: mariangela.demaio@uniroma1.it

rocket engines is extremely important because of the harsh environment to which the system is subjected. The present authors (Nasuti, Torricelli & Pirozzoli 2021) have recently carried out a numerical study of flow in smooth rectangular cooling ducts, and they found that traditional approaches such as Reynolds-averaged Navier–Stokes (RANS) can yield good prediction of the pressure drop. Most studies in ducts have been carried out for the canonical case of circular pipes with smooth walls, which has for instance been the focus of recent numerical studies at high Reynolds number (Pirozzoli *et al.* 2021). The case of rough walls is however at least as important, but so far it has mainly received attention through experimental studies. Recent technological advances in the field of additive manufacturing have further prompted investigations of flow over surfaces with larger relative roughness than the one studied so far (Calignano *et al.* 2013; Snyder *et al.* 2016; Stimpson *et al.* 2016). Additive manufacturing indeed allows one to build three-dimensional objects starting from a digitised three-dimensional model and adding material such as plastics, liquids or powder grains being fused, typically layer by layer. This procedure allows for instance machine cooling channels with more complex geometry and smaller size, however it also yields large relative roughness, which can affect frictional drag significantly. Understanding the behaviour of flows over irregular rough surfaces with higher relative roughness than studied in most experiments is thus certainly of great practical interest.

The systematic experimental investigation carried out by Nikuradse (1933) is widely regarded as the starting point for the study of turbulent flows over rough walls. Nikuradse compiled an extensive database for fully developed flow in circular pipes whose walls were covered with unstructured roughness consisting of sieved sand grains, and found non-monotonic behaviour of the friction factor with change of the Reynolds number. He also noticed that for all the tested surfaces the transition from laminar to turbulent flow occurred roughly at the same critical Reynolds number ($Re_b \approx 2000$). Last, he noticed that in the fully turbulent regime the larger the roughness the higher is the friction factor, whereas in the laminar regime the friction factor of all the tested rough surfaces collapsed to the smooth pipe case. Since reproduction of the exact kind of surface used in Nikuradse's experiments is almost impossible, no later studies succeeded in precisely reproducing his results. Later research on the subject was carried out by Colebrook *et al.* (1939), who investigated flow in commercial galvanised, cast- and wrought-iron pipes, for which the friction factor displayed monotonic decrease with the Reynolds number in the transitionally rough regime. It was generally believed that the different behaviour observed in Nikuradse's and Colebrook's experiments is due to the presence of roughness elements of one size in the former case, whereas it is expected that realistic engineering surfaces which feature roughness elements with disparate sizes should more closely follow Colebrook's trends. However, some recent experimental studies refuted this assumption, showing that a wide range of irregular surfaces more closely follow Nikuradse's behaviour instead of Colebrook's. It is the case for surfaces finished with a honing tool (Schultz & Flack 2007), sanded surfaces (Flack, Schultz & Rose 2012), grit-blasted surfaces (Flack *et al.* 2016) and sandpaper (Flack & Schultz 2023).

Experimental investigations over rough surfaces have mainly been carried out inside plane channels. The only available experimental results concerning pipes with very large relative roughness are due to Huang *et al.* (2013). Those authors studied both the laminar and the turbulent regime and found that the friction factor behaves differently than found by Nikuradse, for high relative roughness. In particular, the transition from the laminar to the turbulent regime was found to occur at bulk Reynolds number less than 2000. Moreover, Huang *et al.* (2013) found that in the laminar region the larger the roughness,

the higher the friction factors, with deviations from the analytical friction formula for the smooth pipe.

Most studies published to date aim at evaluating an equivalent sand-grain roughness height (k_s), for rough surfaces with different geometries. The equivalent sand-grain roughness, first defined by Schlichting (1936), is the size of sand grains in Nikuradse's experiments which yield the same drag as the surface under consideration. The behaviour of rough walls is primarily controlled by the parameter $k_s^+ = k_s/\delta_v$ (where $\delta_v = \nu/u_\tau$, and $u_\tau = (\tau_w/\rho)^{1/2}$ are the viscous length scale and the friction velocity), namely the ratio of the equivalent sand-grain roughness height to the viscous length scale. Based on the value of k_s^+, Nikuradse (1933) identified three flow regimes: hydraulically smooth, transitionally rough and fully rough. In the first regime the height of the roughness is of the order of the viscous sublayer, hence roughness does not affect the flow behaviour. In the transitionally rough regime, the behaviour of the flow instead depends strongly on the geometrical parameters of the roughness. Finally, in the fully rough regime the friction coefficient is nearly unaffected by Reynolds number variations.

The presence of roughness affects both the mean flow and the turbulent motion of a fluid, which entails an increase of friction with respect to the smooth wall case. This is linked to the downward shift in the inner-scaled profile of the mean streamwise velocity, which can be expressed through the roughness function (Clauser 1954; Hama 1954),

$$\Delta U^+ = \frac{1}{\kappa}\log k^+ + A - B(k^+), \tag{1.1}$$

where $\kappa(\approx 0.4)$ is the von Kármán constant, $A(\approx 5.0)$ is the log-law intercept for flow over smooth walls, and B is a function of both the roughness topography and the roughness Reynolds number k^+. The hydraulically smooth regime is realised for small k^+ ($\Delta U^+ \approx 0$). As k^+ increases the roughness function becomes non-zero, and the flow is transitionally rough. In this regime the shape of ΔU^+ in the Nikuradse-type roughness exhibits an inflectional behaviour, whereas it is more gradual in Colebrook-type roughness. The fully rough regime is achieved for $\Delta U^+ > 7$, in which case B becomes independent of k^+, while still depending on the roughness geometry. Hence, the equivalent roughness height can be estimated for any kind of rough surface by making the roughness function collapse to Nikuradse's results in this universal regime. For the so-called k-type roughness (Jiménez 2004), k_s is proportional to k, and their ratio is referred to as the reduction coefficient (Schlichting 1936).

So far, past studies focused on the demonstration of the validity of Townsend's outer-layer similarity hypothesis (Townsend 1976). According to that hypothesis, smooth and rough wall turbulence behave similarly away from the wall at sufficiently high Reynolds number in the presence of sufficient scale separation between the typical roughness height (k) and the outer length scale of the flow (δ, e.g. the pipe diameter). Jiménez (2004) stated that scale separation requires $k/\delta \lesssim 1/40$. However, several studies have shown that outer-layer similarity still holds in the wake region of the wall layer for surfaces with higher relative roughness (Chan *et al.* 2015; Busse, Thakkar & Sandham 2017; Forooghi *et al.* 2017). Jiménez (2004) defined this kind of roughness as 'obstacles', and stated that its behaviour is highly dependent on its geometry.

So far, direct numerical simulations (DNS) have been mainly focused on structured roughness. Leonardi *et al.* (2004) studied the organised motion in a turbulent channel flow with transversal square bars, and Orlandi, Leonardi & Antonia (2006) focused on channel flows with two-dimensional roughness elements of various shapes. They noticed that the wall-normal and spanwise velocity fluctuations increase with respect to the smooth wall

case, whereas the streamwise velocity fluctuations do not, suggesting that isotropy is more closely achieved over a rough wall than over a smooth wall. Only Chan *et al.* (2015) has carried out DNS in a rough pipe, albeit with a specific focus on deterministic, sinusoidal roughness. Those authors found that Townsend's outer-layer similarity was achieved with universality of the first- and second-order statistics, provided $k/\delta \lesssim 1/7$, hence much higher value than proposed by Jiménez (2004).

DNS studies of turbulent flow over irregular roughness have also been recently carried out, limited to the case of flow in plane channels. In a series of studies, Busse *et al.* (2017) and Thakkar, Busse & Sandham (2017, 2018) investigated the flow over many kinds of rough surfaces that were scanned and suitably filtered. Also in this case the behaviour of the friction coefficient was found to be similar to that proposed by Nikuradse. In particular, the roughness function for the grit-blasted surface studied in Thakkar *et al.* (2018) was found to closely follow Nikuradse's results, hence this kind of roughness can be regarded as a digital representation or surrogate for Nikuradse's sand-grain roughness. At the highest Reynolds numbers under consideration ($Re_b \approx 16\,000$), those authors confirmed that Townsend's outer layer similarity was verified, provided $k/\delta \approx 1/6$. Many previous studies have attempted to determine *a priori* correlations between k_s and the geometrical parameters of the roughness. These correlations have been explored in both experimental (Flack & Schultz 2010; Flack *et al.* 2016; Flack, Schultz & Barros 2020) and numerical research (Chan *et al.* 2015; Forooghi *et al.* 2017; De Marchis *et al.* 2020). In a recent study, Jouybari *et al.* (2021) introduced a novel approach by employing deep neural network (DNN) and Gaussian process regression (GPR) techniques.

A comprehensive overview of studies of flow over rough walls has recently been compiled by Chung *et al.* (2021). One of the conclusions of that study is however that 'Effort is required for predicting heat and mass transfer [$\cdots$] and improving our understanding of the influence of topography'. The present work aims at investigating the influence of relatively large roughness on the flow inside circular pipes, with the goal of characterising the flow structure and trying to characterise the equivalent sand-grain roughness, for the case of a grit-blasted surface and a graphite-like surface. A relatively wide range of Reynolds numbers is investigated, up to the fully rough regime, to allow direct comparison with Nikuradse's friction diagram.

2. Methodology

2.1. *Numerical method and definitions*

A second-order finite-difference discretisation of the incompressible Navier–Stokes equations in Cartesian coordinates is used, based on the classical marker-and-cell method (Harlow & Welch 1965; Orlandi 2000), with staggered arrangement of the flow variables to remove odd–even decoupling phenomena and guarantee discrete conservation of the total kinetic energy in the inviscid flow limit. Uniform volumetric forcing is applied to the streamwise momentum equation through a time-varying pressure gradient Π, to maintain constant mass flow rate in time. The Poisson equation resulting from enforcement of the divergence-free condition is efficiently solved by double trigonometric expansion in the streamwise and spanwise directions, and inversion of tridiagonal matrices in the third direction (Kim & Moin 1985). An extensive series of previous studies about wall-bounded flows from this group proved that second-order finite-difference discretisation yields in practical cases of wall-bounded turbulence results which are by no means inferior in quality to those of pseudospectral methods (e.g. Pirozzoli, Bernardini & Orlandi 2016). A hybrid third-order Runge–Kutta algorithm is used for time integration, whereby the

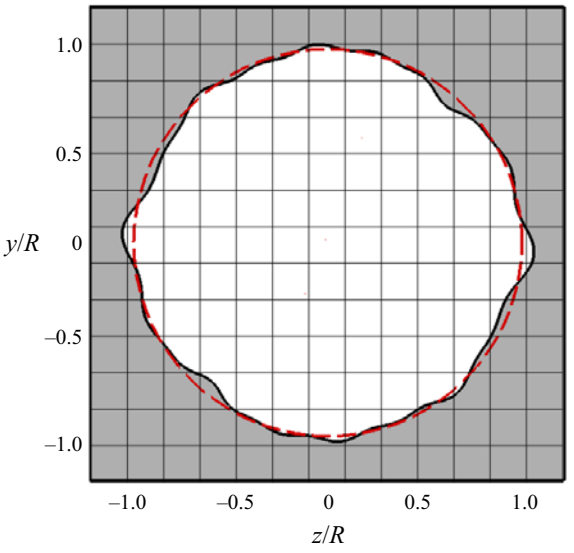

Figure 1. Schematic representation of the grid of a pipe cross section. Black solid lines represent the rough surface boundary, red dashed lines indicates the mean pipe surface.

convective terms are treated explicitly, and the diffusive terms are handled implicitly to alleviate the time step limitation.

The computational domain is a rectangular box of size $L_x \times L_y \times L_z$, covered with a uniform Cartesian mesh, as shown in figure 1 for a representative pipe cross section. A rough pipe with mean radius R and cross-sectional area $A = \pi R^2$ is embedded in it, and the no-slip boundary conditions are approximately enforced through the immersed-boundary method. As a preliminary step, the pipe geometry is generated in the standard Stereo-LiThography format, and a geometrical preprocessor based on the ray-tracing algorithm (O'Rourke *et al.* 1998) is applied to discriminate grid points belonging to the fluid and the solid phase (Iaccarino & Verzicco 2003). Near the fluid–solid interface the viscous terms dominate the nonlinear and pressure terms, hence the boundary conditions can be enforced by locally changing the finite-difference weights for the approximation of the second derivatives (Orlandi & Leonardi 2006). The predictive capability of the method for the numerical simulation of turbulent flows over rough surfaces was documented in a large number of papers (e.g. Iaccarino & Verzicco 2003; Nikitin & Yakhot 2005; Orlandi & Leonardi 2006; Burattini *et al.* 2008; Bernardini, Modesti & Pirozzoli 2016; Orlandi, Modesti & Pirozzoli 2018).

The controlling parameter of the flow is the bulk Reynolds number $Re_b = 2Ru_b/\nu$, where

$$u_b = \frac{1}{V}\int_V U \,\mathrm{d}V, \tag{2.1}$$

is the bulk velocity, with U the mean streamwise velocity and V the fluid volume. The resulting friction Reynolds number is $Re_\tau = Ru_\tau/\nu$, where the friction velocity is evaluated based on the measured pressure gradient, $\tau_w = R/2\langle \Pi \rangle$. Hereafter, uppercase letters are used to denote flow properties averaged in the streamwise direction and in time, lowercase letters denote fluctuations thereof and brackets denote the averaging operator. The $+$ superscript is here used to denote wall units, namely quantities made non-dimensional with respect to the friction velocity and the viscous length scale.

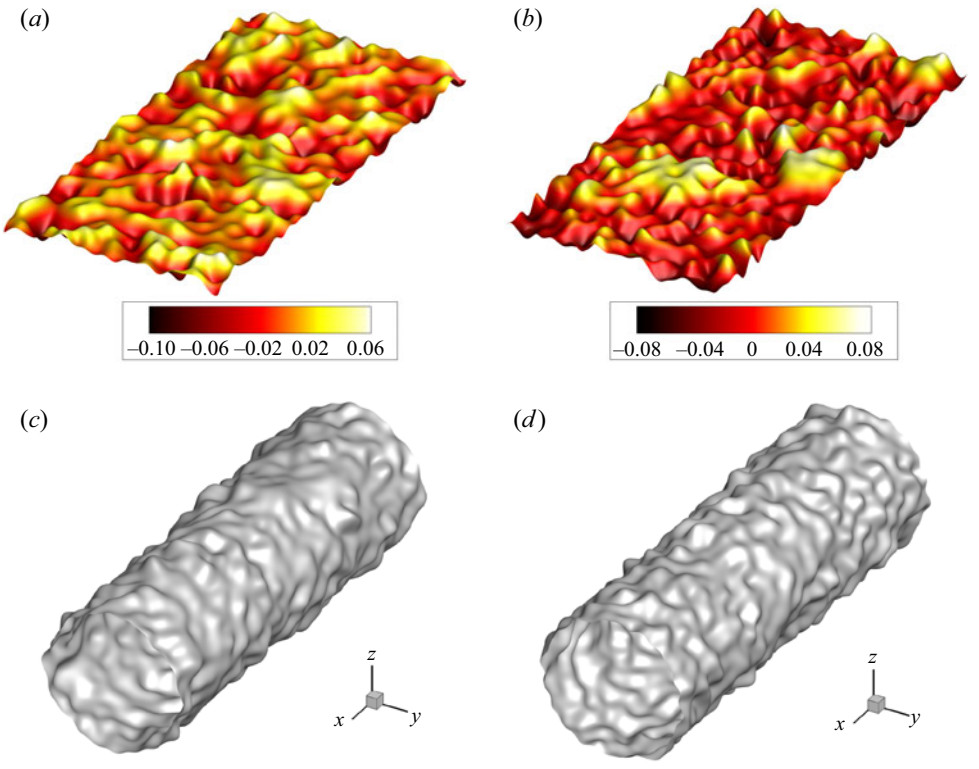

Figure 2. Topography of rough surfaces. Panels (*a*) and (*b*) show the geometries of grit-blasted surface and graphite surface, originally used for channel flow (Thakkar *et al.* 2017), with the colour map showing the elevation normalised by the channel half-height. Panels (*c*) and (*d*) show the geometries obtained by wrapping the original rough surfaces around the pipe as explained in the text.

2.2. *Roughness geometry*

Two types of rough surfaces are considered, both taken from the University of Southampton Institutional Repository (Thakkar, Busse & Sandham 2016). The first, shown in figure 2(*a*), derives from the scan of a grit-blasted surface, and the second, shown in figure 2(*b*), derives from a sample of graphite. In both cases a low-pass Fourier filter was applied to the scanned roughness profiles. This post-processing procedure is necessary as surface scans generate noise which needs to be removed, and because a smoothly varying periodic surface is required to impose periodic numerical boundary conditions in the streamwise direction. Full information about the database is available in Thakkar *et al.* (2017). The rough pipe geometries shown in panels (*c*) and (*d*) were then obtained by doubling the baseline samples in the spanwise direction, and wrapping the surfaces thus obtained around the mean pipe geometry. This procedure guarantees preservation of geometrical similarity of the roughness, while modifying the relative roughness height, which is $1/6$ of the channel half-height for Thakkar *et al.* (2017), and $k/R \approx 1/5$ in our case.

Table 1 displays some relevant geometrical parameters which characterise the resulting roughness. In this study we define the roughness height to be the mean-peak-to-trough height (k), as obtained by partitioning the surface into 5×5 tiles of equal size and then computing the average of the difference between the maximum and minimum height for each tile (Thakkar *et al.* 2017). Other parameters commonly used to quantify roughness

Roughness type	k/R	S_a/R	S_q/R	Sk	$S_{z,max}/R$	ES
Grit-blasted	0.186	0.031	0.040	−0.519	0.293	0.234
Graphite	0.199	0.043	0.045	0.280	0.274	0.279

Table 1. Geometrical properties of the rough pipe surfaces considered in this study.

are the average roughness height,

$$S_a = \sum_{i,j}^{M,N} |h_{i,j}|/(MN), \tag{2.2}$$

and the root-mean-square roughness height,

$$S_q = \sqrt{\sum_{i,j}^{M,N} h_{i,j}^2/(MN)}, \tag{2.3}$$

where $h_{i,j}$ are roughness heights obtained after the filtering procedure, and M and N are the number of data points in the streamwise and spanwise directions. Other relevant parameters include the skewness,

$$Sk = \sum_{i,j}^{M,N} h_{i,j}^3/(MNS_q^3), \tag{2.4}$$

and the maximum peak-to-trough height,

$$S_{z,z,max} = max(h_{i,j}) - min(h_{i,j}). \tag{2.5}$$

The last parameter reported in table 1 is the effective slope, defined as

$$ES = \frac{1}{L_x L_y} \int_0^{L_x} \int_0^{L_y} \left| \frac{\mathrm{d}h}{\mathrm{d}x} \right|_{i,j} \mathrm{d}x\,\mathrm{d}y, \tag{2.6}$$

where L_x and L_y are the dimensions of the baseline smooth surface along the streamwise and spanwise directions.

The pipe length is about $L_x = 6.27R$, in both cases. The computational domain in the cross-stream directions measures $L_y = L_z = 2.45R$, for the grit-blasted surface, and $L_y = L_z = 2.29R$, for the graphite surface, such that the roughness is wholly confined. Preliminary studies have been carried out to establish the sensitivity of the computed results on the length of the pipe. DNS in axially doubled domains have in fact shown that, for given grid resolution, the friction factor $f = 8\tau_w/(\rho u_b^2)$ (and other key statistics) varies by no more than 1 %. Hence, the baseline domain only is considered from now on. It is also important to note that in the forthcoming presentation of the results, the wall distance y is measured from the roughness centroid, hence negative y are allowed. We set $y = 0$ corresponding to the mean pipe radius, in such a way to achieve collapse of the total stress to the smooth-wall case (Chan *et al.* 2015; Thakkar 2017), as shown in § 3.2. Although alternative definitions of the virtual origin are possible, for instance in terms of the height of the roughness at which the integrated resultant force acts (Chan *et al.* 2015), that is impossible to implement within the immersed-boundary approach which we use.

Re_b	Re_τ	k^+	$f \times 10^2$	N_x	$N_y = N_z$	Δx^+	$\Delta z^+ = \Delta y^+$	T/τ_t	Symbol
				Grit-blasted					
500	32.75	6.08	13.72	384	192	0.53	0.42	104.77	
1000	46.69	8.70	6.98	384	192	0.76	0.60	74.70	
1500	58.41	10.89	4.85	384	192	0.96	0.75	62.29	
1750	64.78	12.03	4.41	384	192	1.06	0.83	59.40	
2500	123.73	23.07	7.81	384	192	2.01	1.58	79.05	
3000	149.88	27.94	7.99	384	192	2.45	1.92	79.94	●
4400	224.75	41.90	8.35	384	192	3.68	1.88	81.73	●
9800	521.67	97.25	9.07	960	480	3.41	2.67	85.17	●
30 000	1613.66	300.14	9.24	1024	512	9.88	7.72	84.38	●
				Graphite					
500	33.21	6.61	14.12	384	192	0.54	0.40	106.28	
1000	47.92	9.53	7.35	384	192	0.78	0.57	76.68	
1250	56.73	11.29	6.60	384	192	0.93	0.68	72.66	
1500	73.20	14.55	7.62	384	192	1.20	0.87	78.08	
2000	104.23	20.72	8.69	384	192	1.70	1.25	83.38	
2500	133.26	26.49	9.09	384	192	2.18	1.59	85.29	
3000	162.69	32.34	9.41	384	192	2.66	1.94	86.77	○
4400	244.54	48.61	9.88	384	192	3.99	2.92	88.92	○
6000	339.51	67.49	10.25	512	256	3.70	2.70	90.54	
9800	570.97	113.50	10.86	960	480	3.73	2.73	93.22	○
30 000	1726.4	343.20	10.56	1152	576	9.40	6.87	92.07	○

Table 2. Flow parameters for flow in pipes with rough walls. The first set of parameters pertains to the grit-blasted surface. In these cases the computational box dimensions are $6.28R \times 2.45R \times 2.45R$. The second set of parameters pertains to the graphite surface, and the box dimensions are $6.27R \times 2.29R \times 2.29R$. Here $Re_b = 2Ru_b/\nu$ is the Reynolds number, $Re_\tau = Ru_\tau/\nu$ is the friction Reynolds number, $k^+ = ku_\tau/\nu$ is the roughness Reynolds number, $f = 8\tau_w/(\rho u_b^2)$ is the friction factor and N_x, N_y and N_z denote the number of grid points in the streamwise, and the two cross-stream directions. Finally, Δx^+, Δy^+ and Δz^+ are the grid spacings in the streamwise and cross-stream directions, given in wall units, T is the time interval used to collect the flow statistics and $\tau_t = R/u_\tau$ is the eddy turnover time.

Establishing the appropriate grid resolution in numerical simulations of turbulence over rough wall is a very important and tricky subject, as discussed by Busse, Lützner & Sandham (2015). In particular, those authors noticed that at least 12 grid points per roughness feature should be used for accurate characterisation of roughness effects. In order to address this issue, we have carried out a grid sensitivity analysis at $Re_b = 4400$, for both roughness geometries, which has shown that at least $N_x = 384$ grid points should be used along the streamwise direction, and $N_y = N_z = 192$ grid points should be used in the transversal directions, which would correspond to about 15 grid points per roughness element, thus corroborating the findings of Busse *et al.* (2015). The results of the grid sensitivity analysis for the grit-blasted surface are shown in the Appendix.

DNS for the two rough pipe geometries have been carried out for a wide range of Reynolds numbers, from $Re_b = 500$ to $Re_b = 30\,000$, with test conditions listed in table 2. The number of grid points has been progressively increased with the Reynolds number. A grid sensitivity analysis has been carried out also for the graphite surface at $Re_b = 30\,000$ (in which a fully rough regime is established), to verify that the uncertainty in the key parameters (f, k^+) is acceptable. The time step expressed in wall units (ν/u_τ^2) ranges from about $\Delta t^+ = 0.015$ for the cases at $Re_b = 500$ to about $\Delta t^+ = 0.29$ for

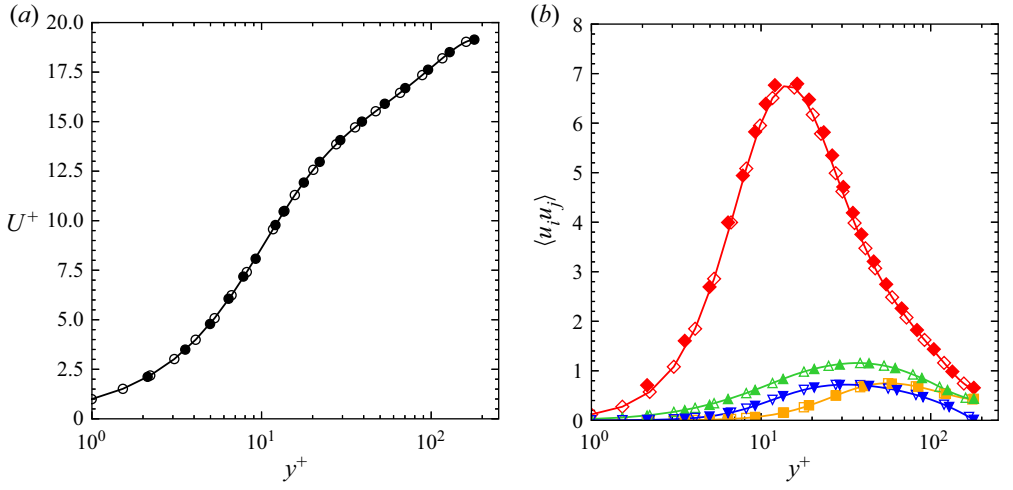

Figure 3. DNS of flow in a smooth pipe: (*a*) mean streamwise velocity U^+; (*b*) velocity variances $\langle u_x^2 \rangle$ ($\diamondsuit$), $\langle u_r^2 \rangle$ ($\square$), $\langle u_\Theta^2 \rangle$ ($\triangle$) and the average of fluctuations product $\langle u_x u_r \rangle$ (∇). Filled symbols denote results of the present DNS and open symbols denote those obtained by Pirozzoli *et al.* (2021). The directory including the data and the Jupyter notebook can be accessed at https://www.cambridge.org/S0022112023007280/JFM-Notebook/files/Figure-3/velocity_validation_smooth.ipynb.

the cases at $Re_b = 30\,000$. The time intervals used to collect the flow statistics are also reported in table 2 in terms of eddy-turnover times ($\tau_t = R/u_\tau$), are typically much longer than the current practice in DNS of smooth channels and pipes (Hoyas & Jimenez 2006; Pirozzoli *et al.* 2021), for the sake of achieving convergence of the statistical properties in the cross-stream plane.

2.3. *Validation*

Preliminary validation of the code was carried out by simulating the flow inside a smooth pipe at $Re_b = 5300$. The results have been compared with those obtained by Pirozzoli *et al.* (2021), using a body-fitted solver for cylindrical coordinates. Figure 3 depicts the profiles of the streamwise velocity and of the velocity variances and turbulent shear stress. The results are quite satisfactory, as the computed Re_τ differ by less than 1 %, and the profiles of the statistical quantities are in very good agreement.

Additional validation included reproducing some DNS results for flow in a plane channel (Busse *et al.* 2017; Thakkar *et al.* 2018). Two Reynolds numbers ($Re_\tau = 180$ and 360) have been considered for each type of roughness, and the key results are presented in table 3. Figure 4 also compares profiles of the mean streamwise velocity, and the roughness function as a function of the roughness Reynolds number. In this respect we must specify that we have re-evaluated the data of Busse *et al.* (2017), since we define the roughness function based on the difference of the velocity profiles within the overlap layer Hama (1954), whereas those authors considered the difference of the centreline values. The results are in general good agreement, difference of the computed Re_τ being no larger than 2 %. This discrepancy is however noticeable in the diagram of the roughness function. A thorough grid sensitivity study has thus been carried out, which has shown no hint of lack of sufficient resolution, hence we believe that remaining differences could be due to different implementation of the immersed-boundary technique.

Simulation	Re_b	Re_τ	U_b/u_τ	k^+	ΔU^+	N_x	N_y	N_z	Symbols
Smooth									
Present study	5700	178.5	15.97	–	–	192	192	256	●
Thakkar *et al.* (2018)	5700	180	15.83	–	–	196	196	140	○
Grit-blasted surface									
Present study	4153	177	11.73	29.5	4.20	384	256	192	▲
Busse *et al.* (2017)	4153	180	11.54	30	4.29	320	288	160	△
Present study	8002	358	11.16	59.67	5.82	512	256	256	▲
Busse *et al.* (2017)	8002	360	11.11	60	5.96	432	576	216	△
Graphite surface									
Present study	3959	178	11.11	29.67	4.73	384	384	192	■
Busse *et al.* (2017)	3959	180	11.00	30	4.87	384	256	192	□
Present study	7544	353	10.64	58.83	6.34	512	512	256	■
Busse *et al.* (2017)	7544	360	10.48	60	6.64	512	512	256	□

Table 3. Results of the validation study for smooth and rough plane channels.

3. Results for rough pipes

The key one-point flow statistics are hereafter reported, as obtained by averaging in time and in the streamwise direction, limited to the volume occupied by the fluid. Figure 5 depicts the mean streamwise velocity distribution over the cross section of the pipe, also within the roughness. Owing to the large relative roughness, the fields do not show any symmetry, thus confirming that for $R/k \lesssim 40$ the effect of the wall is felt throughout the wall layer (Jiménez 2004). Furthermore, according to Chung *et al.* (2021) and Jelly *et al.* (2022), the diameter and the strength of the secondary flows is sensitive to the spanwise length scale of the roughness in proportion to the outer scale of the problem, say δ. Specifically, Chung *et al.* (2021) state that the diameter of the secondary flows is about δ when the spanwise wavelength of the roughness matches or exceeds the outer scale, here the pipe radius. In the present study, the longest azimuthal wavelength is half the circumference of the pipe. Consequently, the lack of axisymmetry in the velocity field even far from the wall might just as well be due to the large azimuthal length scale, which yields a large secondary flow. Furthermore, the velocity isolines show clear sensitivity to Reynolds number variations and to the roughness geometry.

Figure 6 depicts the wall-normal profiles of the streamwise velocity, obtained by further averaging in the azimuthal direction. The figure shows that increase of k^+ yields a downward shift of the velocity profiles with respect to the case of a smooth pipe, thus yielding a larger roughness function. Near the wall, the behaviour is the opposite, as DNS at higher k^+ have higher mean velocity, since the flow is capable of penetrating deeper into the roughness canopy (Busse *et al.* 2017; Thakkar *et al.* 2018). Despite the high relative roughness, a logarithmic layer can still be identified in all cases, with slope similar to the smooth wall case, which allows us to consistently define a roughness function.

Figure 7 shows the same velocity profiles in defect form. Some scatter is, in fact, observed away from walls (say, $y/R \gtrsim 0.2$), for both roughness geometries, which however tends to be reduced as Re grows. In particular, the grit-blasted surface seems to exhibit collapse to the smooth wall velocity profile once a fully rough regime is attained, with 4 % deviations at most, at $Re_b = 30\,000$. Poorer collapse observed in the case of the graphite

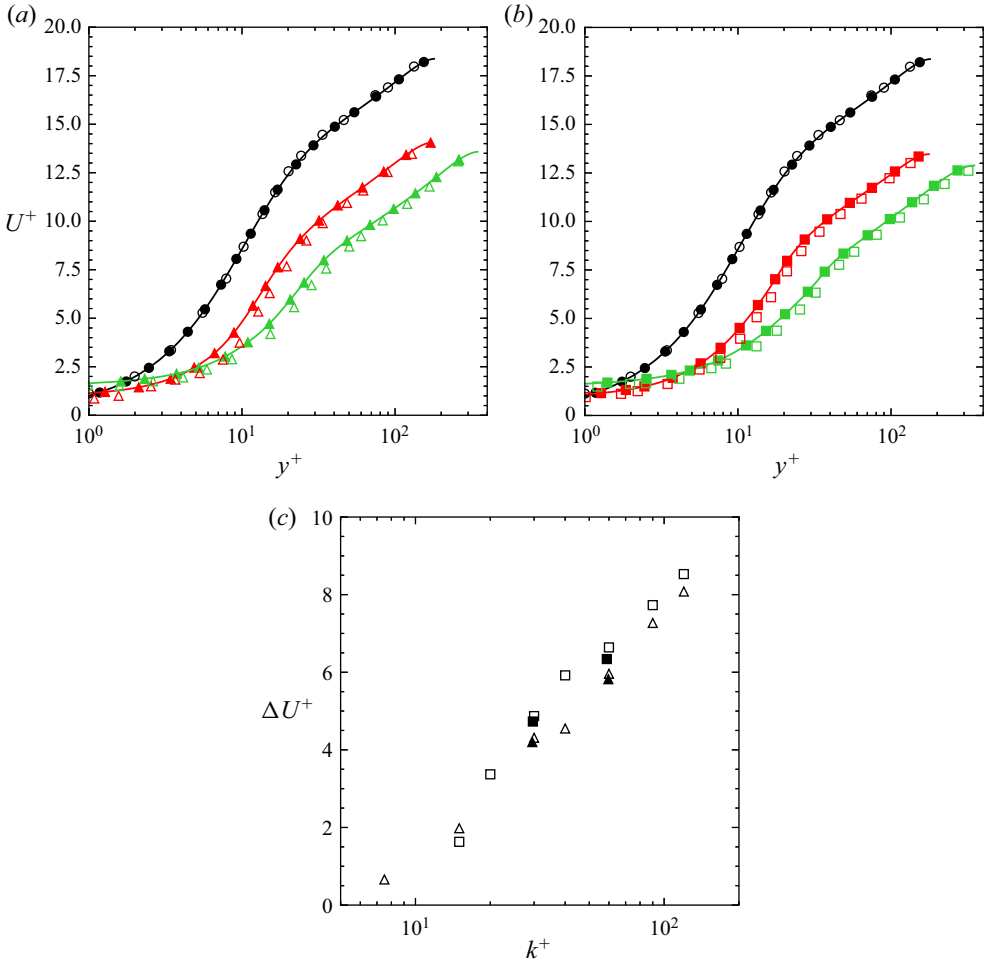

Figure 4. DNS of flow in rough channel: mean streamwise velocity U^+ for grit-blasted (*a*) and graphite (*b*) (symbols as in table 3); (*c*) roughness function as a function of roughness Reynolds number (symbols as in table 3). The directory including the data of the profiles and the Jupyter notebook can be accessed at https://www.cambridge.org/S0022112023007280/JFM-Notebook/files/Figure-4a-b/channel_validation.ipynb. The roughness functions and the Jupyter notebook can be accessed at https://www.cambridge.org/S0022112023007280/JFM-Notebook/files/Figure-4c/deltau.ipynb.

surface could be due to higher relative roughness, In that case, deviation are 13 % at most, at $Re_b = 30\,000$. Validity of Townsend's outer-layer similarity for the velocity profile over structured and unstructured rough surfaces was previously documented by Orlandi & Leonardi (2006), Busse *et al.* (2017), Thakkar *et al.* (2018), MacDonald, Hutchins & Chung (2019), Flack, Schultz & Shapiro (2005) and Jiménez (2004). Despite large relative roughness, our DNS provides evidence that close similarity is achieved even at $k/R \approx 1/5$. Given the severe non-uniformities observed in figure 5, the fact that the azimuthally averaged velocity profiles still bear close resemblance to those found in the case of smooth walls further points to the importance of the imposed spatially uniform pressure gradient, rather than the local wall conditions. Similar observations were reported by Pirozzoli *et al.* (2018) for flow in smooth square ducts.

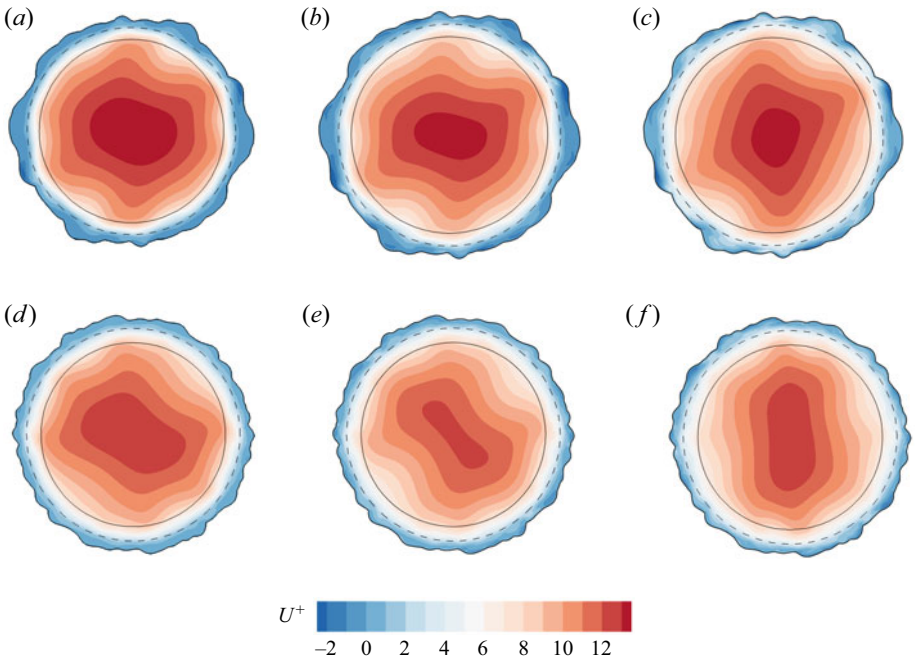

Figure 5. Contours of mean streamwise velocity for the grid-blasted surface (*a–c*) and the graphite surface (*d–f*), with symbols referring to the flow conditions in table 2: (*a*) • orange; (*b*) • green; (*c*) • blue; (*d*) ○ orange; (*e*) ○ green; and (*f*) ○ blue. The dashed line marks the mean pipe surface and the solid line marks the plane of the crests. The boundary of the maps corresponds to points beyond which no fluid element if found.

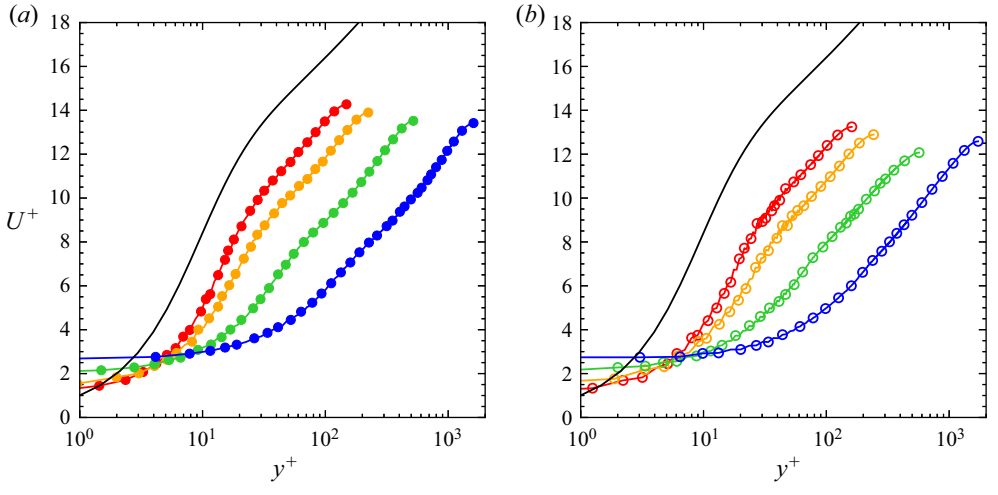

Figure 6. Profiles of streamwise velocity for the grit-blasted surface (*a*) and the graphite surface (*b*) at various Reynolds numbers, symbols as in table 2. The black line corresponds to the smooth wall case. The directory including the data of the profiles and the Jupyter notebook can be accessed at https://www.cambridge.org/S0022112023007280/JFM-Notebook/files/Figure-6/velocity.ipynb.

3.1. *Friction*

In figure 8 the friction factors obtained from the present DNS are superposed to Nikuradse's chart, with the obvious caveat that the relative roughness in those experiments is much less than in our case. Referring to the laminar flow region in the low-*Re* end of

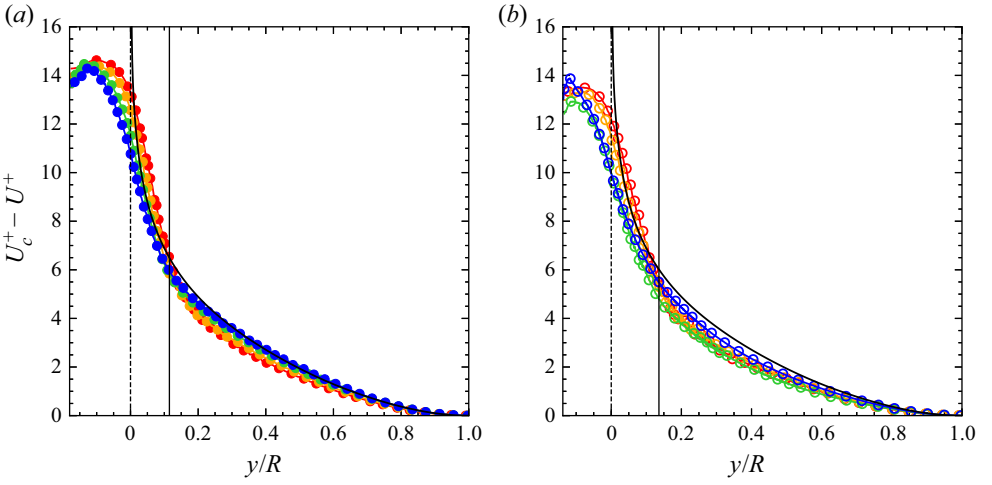

Figure 7. Velocity defect profiles ($U_c^+ - U^+$, with U_c the mean centreline velocity) for the grit-blasted surface (a) and the graphite surface (b) at various Reynolds numbers, with symbols defined in table 2. The black line corresponds to the smooth wall case. The vertical solid line corresponds to the plane of the crests and the dashed line marks the roughness centroid $y/R = 0$. The directory including the data of the profiles and the Jupyter notebook can be accessed at https://www.cambridge.org/S0022112023007280/JFM-Notebook/files/Figure-7/velocity_defect.ipynb.

the graph, in Nikuradse's experiments the friction factor for all surfaces collapsed to the Hagen–Poiseuille prediction $f = 64/Re_b$, thus suggesting that friction is not affected by the change of the wall geometry. In the present DNS we find instead that the computed friction factors are higher than the expected theoretical values by about 5–9 %. This indicates that in our case the larger relative roughness has the role of altering the geometry of the pipe, thus producing modification also in the laminar flow regime. Similar findings where reported by Huang *et al.* (2013), who found that deviations from the viscous theory appears for relative roughness of about 14 %. In that study, Huang *et al.* (2013) carried out the experiments by considering a pipe with wall covered with spheres of various diameter to simulate roughness with different height. In that case, the relative roughness height was defined as the ratio between the diameter of the spheres and the radius of the pipe without the spheres.

The large relative roughness in the pipe geometries under consideration has the intuitive effect of reducing the available pipe area for fluid flow, thus the effective radius of the pipe is smaller than the geometrical mean radius. Kandlikar *et al.* (2005) defined the effective radius of the pipe by subtracting the average roughness height from the mean radius, however in that case the effective radius would change according to the definition of the average roughness height, which is not universal. In the present study, we define the effective radius to be the hydraulic radius, which is traditionally used for friction prediction in non-circular ducts, and defined as $R_h = 2V/S$, where V is the volume occupied by the fluid and S is the area of the wetted surface. Figure 8(b) shows the Nikuradse diagram obtained by replacing Re_b with $Re_h = 2R_h u_b/\nu$. In this representation we find that the results collapse to the Hagen–Poiseuille prediction to within less than 1 %.

Huang *et al.* (2013) also noticed that the larger the relative roughness, the lower the Reynolds number at which transition from laminar to turbulent regime occurs. This prediction is corroborated by the present data, and in fact transition occurs earlier for the graphite surface than the grit-blasted surface, on account of higher relative roughness.

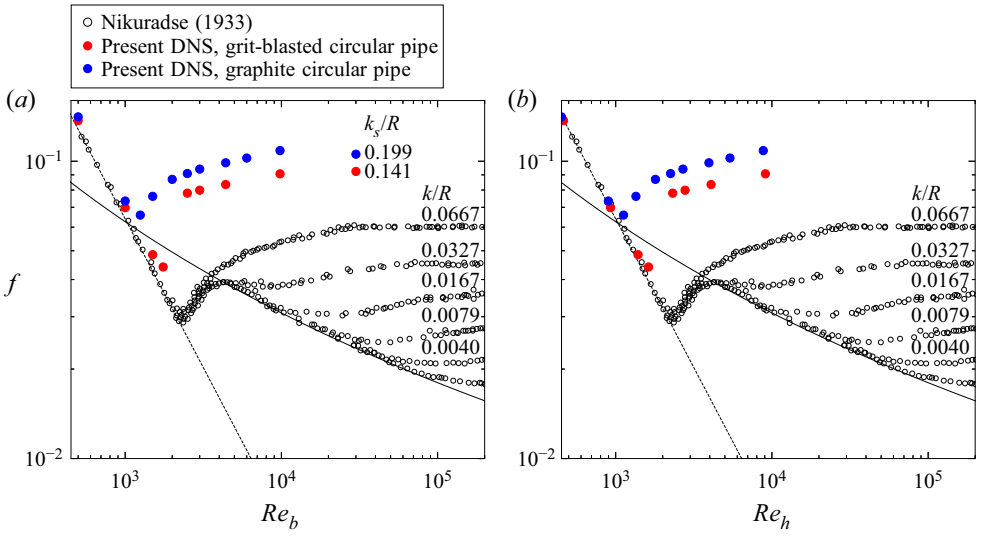

Figure 8. (*a*) Variation of friction factor (f) with bulk Reynolds number (Re_b) based on the mean radius (R). (*b*) Variation of friction factor with the effective bulk Reynolds number (Re_h) based on the effective radius (R_h). Nikuradse's data are shown for pipes with various relative roughness height (k/R). The dashed line denotes the Hagen–Poiseuille $f = 64/Re_b$ friction law and the solid line denotes the Prandtl friction law for turbulent pipe flow. The directory including the data and the Jupyter notebook can be accessed at https://www.cambridge.org/S0022112023007280/JFM-Notebook/files/Figure-8/Nikuradse.ipynb.

Transition is found to occur similarly (but perhaps more sharply) than in Nikuradse's experiments. Most interestingly, the friction factor past the transition point is found to increase with the Reynolds number, consistent with numerical simulations in channels with the same roughness geometry (Busse *et al.* 2017). However, the behaviour in this regime is known to be significantly affected by the nature of the roughness (Colebrook *et al.* 1939; Jiménez 2004; Flack *et al.* 2012, 2020). Evidence for the establishment of a fully rough regime is found at the highest Reynolds numbers considered, which show very small variation of the friction factor (also see table 2).

In figure 9(*a*) we show the roughness function for our DNS (determined based on the log-law shift) as a function of k^+. In the figure we also show data from the channel flow DNS of Busse *et al.* (2017), from Nikuradse's experiment (Nikuradse 1926) and Colebrook's relation (Colebrook *et al.* 1939)

$$\Delta U^+ = 1/\kappa \log(1 + 0.3k^+). \tag{3.1}$$

The procedure which we use to determine the roughness function relies on comparing the mean velocity profiles for a rough pipe with the mean velocity profile for a smooth pipe at the same (or similar) Re_τ, using the database of Pirozzoli *et al.* (2021). We visually identify a log layer, and then determine the additive constant by fitting the data with a logarithmic function with prefactor $1/\kappa$, following the approach of Orlandi & Leonardi (2006), and as illustrated in figure 10.

When reported as a function of k^+, the roughness function has a trend quite similar to that observed in Nikuradse's experiments, and consistent with the channel flow DNS of Busse *et al.* (2017), whereas data depart from Colebrook's relation at $k^+ \lesssim 50$. Consistent with observations made regarding the friction chart, we find that our data exceed $\Delta U^+ = 7$, which is the commonly accepted threshold for achievement of the fully rough regime. In the fully rough region, the difference of the roughness function in pipe

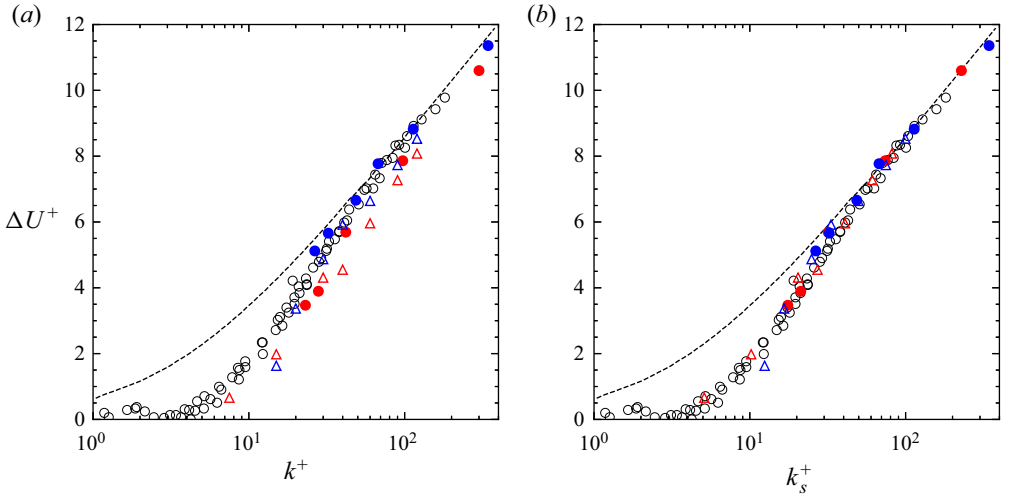

Figure 9. Variation of roughness function with inner-scale roughness height (*a*) and with equivalent sand-grain roughness height (*b*). The dashed line denotes Colebrook's relation (Colebrook *et al.* 1939), $\Delta U^+ = 1/\kappa \log(1 + 0.3k_s^+)$. The solid circles denote data from the present DNS: red, grit-blasted surface; blue, graphite surface. The open circles denote values taken from Nikuradse's experiment, and the triangles results of Busse *et al.* (2017), for grit-blasted surface (red) and graphite surface (blue). The directory including the data of the profiles and the Jupyter notebook can be accessed at https://www.cambridge.org/S0022112023007280/JFM-Notebook/files/Figure-9.

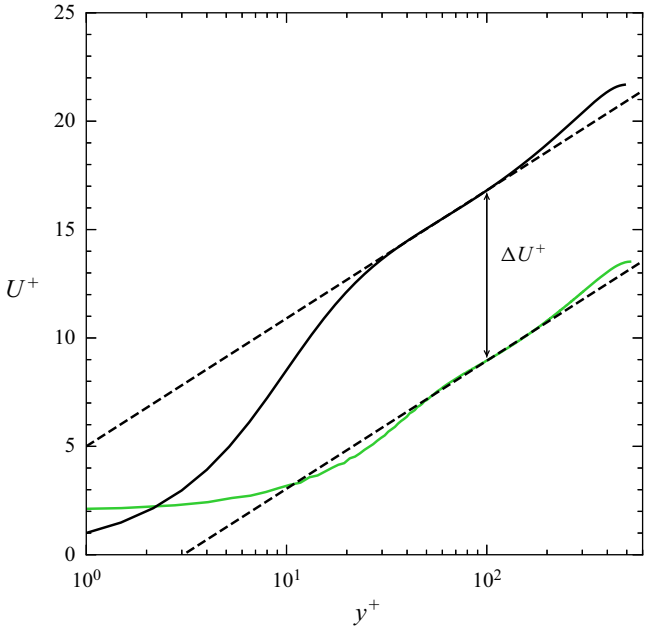

Figure 10. Procedure for determination of the roughness function: mean streamwise velocity profiles for grit-blasted surface at $Re_b = 9800$ (green line), compared with smooth pipe at $Re_\tau = 495$ (black line). The dashed lines denote the functional relation $U^+ = 1/0.39 \log y^+ + A$, with $A = -2.86$ and $A = 5$, respectively, as resulting from data fitting.

and channel flow for given roughness is about 5 %, which points to the non-negligible effect of the duct geometry in the presence of large roughness as in the present case. As is customary (Jiménez 2004) we proceed to determine values of the equivalent sand-grain roughness height, by enforcing universality of the roughness function to the fully rough asymptote of (3.1). Data fitting of our DNS results yields $k_s^+ \approx 0.76k^+$ for the grit-blasted surface, and $k_s^+ \approx 1.0k^+$ for the graphite sample. Data fitting of the channel flow DNS results of Busse *et al.* (2017) yields instead $k_s^+ \approx 0.68k^+$ for the grit-blasted surface, and $k_s^+ \approx 0.83k^+$ for the graphite sample. Once the roughness function is plotted against k_s^+, we note that the trend of ΔU^+ collapses to Nikuradse's results throughout, which is an indication that both surfaces under consideration behave as Nikuradse's roughness. In order to analyze the behaviour at yet lower k_s^+, we should use a very low Reynolds number, given the large value of k/R in our roughness. However at low Re it is difficult to define a proper logarithmic region to consistently evaluate the roughness function. Another approach would be to consider lower k/R, which however would make the simulations computationally much more demanding.

3.2. *Statistics of velocity fluctuations*

In figure 11 we show the distribution of the velocity variances as a function of the outer-scaled wall distance. For reference, data for smooth pipes (Pirozzoli *et al.* 2021) are also shown at various Re_τ. Regarding the streamwise velocity variance, the structure is overall similar to the smooth wall case, with a near-wall peak associated with the presence of streaks. However, the amplitude of the peak is less than in the smooth case, for given Re_τ, which is an indication that roughness tends to disrupt the classical near-wall cycle of turbulence regeneration (Orlandi *et al.* 2006), diverting kinetic energy from the streamwise direction to the other velocity components. We further find that as the Reynolds number increases, the near-wall peak is shifted outwards, suggesting that turbulent structures can penetrate deeper into the roughness canopy. On the other hand, the amplitude of the peak is barely affected, especially in the case of the graphite surface. This might point to modifications of outer-layer influences (Townsend 1976; Marusic, Baars & Hutchins 2017), or more probably to compensation between decrease resulting from higher k^+, and decrease due to logarithmic increase with Re_τ resulting from outer eddies. Our results also corroborate the findings of Busse & Sandham (2012) and De Marchis, Napoli & Armenio (2010), who reported decrease of the streamwise variance peak with the roughness function. The distributions of the wall-normal and azimuthal velocity variances also support the notion that rough walls disrupt the turbulence structures close to walls (Orlandi & Leonardi 2006; De Marchis *et al.* 2010), increasing isotropy of the turbulent stresses. In fact, our data show clear growth of $\langle u_r^2 \rangle$ and $\langle u_\Theta^2 \rangle$ as Re grows, and near isotropy of the wall-parallel velocity fluctuations is achieved at the highest Reynolds number under scrutiny. Figure 11(*g*,*h*) depicts the distribution of the turbulent shear stress, $\langle u_x u_r \rangle$. As is the case of smooth walls, deviations from the linear behaviour of the total stress are observed as the wall is approached, because of increasing importance of viscous stresses. As the Reynolds number increases, we find that the peak value of the shear stress increases more significantly than in the smooth wall case. This is due to greater turbulent activity within the roughness canopy, as also suggested by the fact that the peak position shifts well inside the plane of the crests.

The above observations are made more quantitative in figure 12, where we show the peak velocity variances as a function of Re_τ, for both smooth walls and for rough surfaces. The figure confirms that the logarithmic increase of the peak streamwise variance is

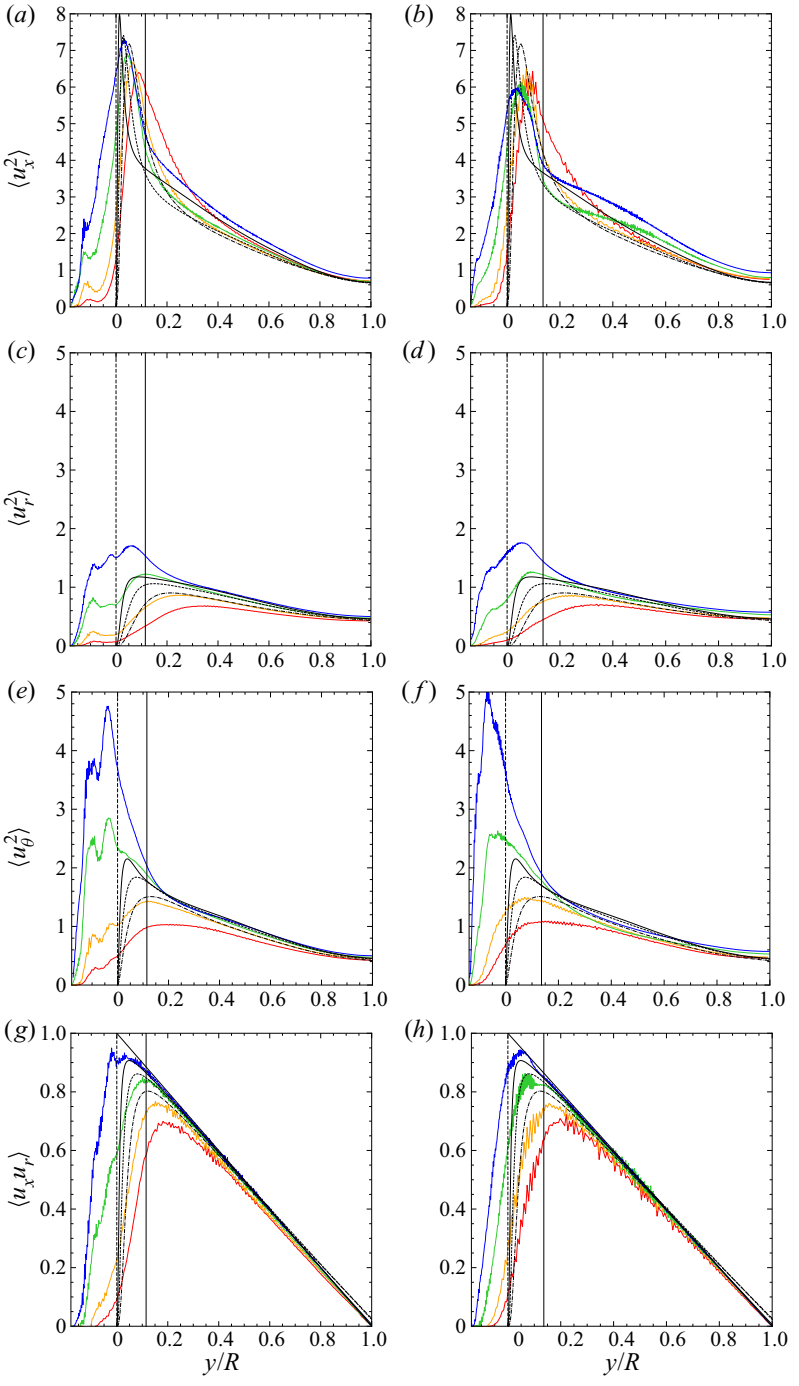

Figure 11. Profiles of velocity variances (streamwise, (*a*,*b*); wall-normal, (*c*,*d*); azimuthal, (*e*,*f*)) and turbulent shear stress (*g*,*h*) for the grit-blasted surface (*a*,*c*,*e*) and the graphite surface (*b*,*d*,*f*) at various Reynolds number. Line colours are defined in table 2. The black lines denote the case of smooth pipes at $Re_\tau = 300$ (dot-dashed line), $Re_\tau = 535$ (dashed line) and $Re_\tau = 1130$ (solid line). The vertical solid line corresponds to the plane of the crests and the dashed vertical line marks the roughness centroid $y/R = 0$. The directory including the data and the Jupyter notebook can be accessed at https://www.cambridge.org/S0022112023007280/JFM-Notebook/files/Figure-11/grit-blasted for the grit-blasted surface and at https://www.cambridge.org/S0022112023007280/JFM-Notebook/files/Figure-11/graphite for the graphite surface.

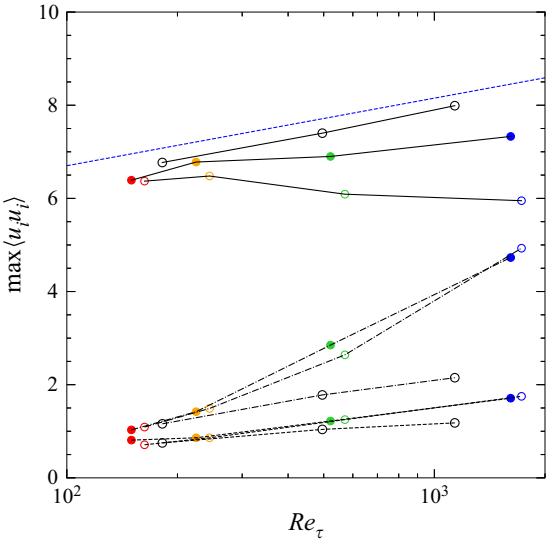

Figure 12. Peak values of velocity variances (streamwise, solid line; wall-normal, dashed line; azimuthal, dot-dashed line) for smooth pipe (open circles), and for grit-blasted and graphite surfaces (symbols as in table 2), at various Reynolds numbers. The blue dashed line denotes the logarithmic law of Marusic *et al.* (2017) for pipes with smooth walls ($\max\langle u_x^2\rangle^+ = 0.63 \log Re_\tau + 3.8$). The directory including the data and the Jupyter notebook can be accessed at https://www.cambridge.org/S0022112023007280/JFM-Notebook/files/Figure-12/fluctuation_peaks.ipynb.

inhibited in the case of a rough surface, whereas the growth rate is higher for the two other fluctuating velocity components. Hence, it appears that the asymptotic state of turbulence over a rough surface should be of two-component type (Lumley 1979; Pope 2000), with the wall-normal velocity still impeded by the impermeability condition. Regarding the behaviour in the outer layer, our DNS data suggest a similar behaviour as in the smooth case, with wall-normal and azimuthal fluctuations which are unaffected by Reynolds number variation, whereas the streamwise fluctuations tend to increase slightly. This again supports validity of Townsend's similarity hypothesis for the velocity fluctuation statistics, to within 14 % deviations.

4. Equivalent sand-grain roughness height

One of the key outstanding engineering goals is the prediction of the equivalent roughness height for given roughness texture, which is an open research problem attracting the attention of many scientists (Chung *et al.* 2021). In table 4 we consider several predictive formulae, mainly based on empiricism, and compare them with k_s resulting from the DNS data, as obtained by collapsing the roughness function to Nikuradse's results in the fully rough regime. The first correlation (Flack & Schultz 2010) was developed using mainly surfaces with positive skewness (sandpaper, gravel and commercial steel pipes) and it does not seem to predict k_s properly neither for the grit-blasted and the graphite surfaces. The correlation reported by Flack *et al.* (2016) was developed from experiments exploiting many grit-blasted surfaces with negative skewness. Versions (*a*) and (*b*) of that correlation differ in that the latter was developed after a filtering procedure is applied to the scanned surface. Indeed, any surface may have waviness which affects the surface parameters but does not contribute to frictional drag, and to address this potential

Correlations	
Flack & Schultz (2010)	$k_s = 4.43S_q(1+Sk)^{1.37}$
Flack *et al.* (2016) (*a*)	$k_s = 2.91S_q(2+Sk)^{-0.284}$
Flack *et al.* (2016) (*b*)	$k_s = 3.47S_q(2+Sk)^{-0.405}$
Flack *et al.* (2020)	$\begin{cases} k_s = 2.73S_q(2+Sk)^{-0.45} & \text{if } Sk < 0 \\ k_s = 2.11S_q & \text{if } Sk = 0 \\ k_s = 2.48S_q(1+Sk)^{2.24} & \text{if } Sk > 0 \end{cases}$
Chan *et al.* (2015)	$k_s = 7.3S_aES^{0.45}$
Forooghi *et al.* (2017)	$k_s = k(0.67Sk^2 + 0.93Sk + 1.3)[1.07(1-\mathrm{e}^{-3.5ES})]$
De Marchis *et al.* (2020)	$\Delta U^+ = \frac{1}{\kappa}\log(ESS_q{}^+) + 3.5$

	Grit-blasted			Graphite		
Correlation	k_s/R	DNS	Error %	k_s/R	DNS	Error %
Flack & Schultz (2010)	0.065	0.14	−53.90	0.276	0.20	38.70
Flack *et al.* (2016) (*a*)	0.104	0.14	−26.24	0.103	0.20	−48.2
Flack *et al.* (2016) (*b*)	0.118	0.14	−16.31	0.111	0.20	−44.2
Flack *et al.* (2020)	0.092	0.14	−34.35	0.192	0.20	−3.5
Chan *et al.* (2015)	0.117	0.14	−16.43	0.175	0.20	−11.60
Forooghi *et al.* (2017)	0.110	0.14	−21.98	0.215	0.20	8.04
De Marchis *et al.* (2020)	0.126	0.14	−10.64	0.162	0.20	−18.59
Jouybari *et al.* (2021) (DNN)	0.041	0.14	−70.92	0.147	0.20	−26.13
Jouybari *et al.* (2021) (GPR)	0.105	0.14	−25.53	0.186	0.20	−6.53

Table 4. Comparison of correlations for the equivalent sand-grain roughness height with DNS data.

issue a long-wavelength filter was applied by those authors. This modification actually appears to yield some improvement over the baseline (*a*) formulation, especially for the grit-blasted surface, for which the predicted error is about 16 %. As expected, errors are larger for the graphite surface, which has positive skewness. The correlation of Flack *et al.* (2020) was developed by studying the flow over synthetically generated surfaces whose parameters could be systematically adjusted to identify the roughness parameters which contribute to drag most. This correlation yields the best estimate of k_s for the graphite smaller than that considered in this study. Chan *et al.* (2015) developed a correlation for sinusoidal roughness, by systematically investigating the influence of wavelength and roughness height, up to $k/D = 1/7$. The main drawback of that study is that only a narrow range of Sk was considered, around zero. As a result, that correlation tends to under-predict k_s for both the grit-blasted and the graphite surfaces, with an error of 17 % at most. Forooghi *et al.* (2017) developed a correlation for k_s based on the analysis of the surface, with a difference of about 3.5 % with respect to the DNS. The large overall errors resulting from the above correlations are likely due to essential differences in the roughness geometry, but also to the use of large roughness in the present DNS. In fact, the largest relative roughness used by Flack and coworkers was about four times the flow over positively skewed surfaces with roughness elements of prescribed shape with both regular and irregular arrangement and size distribution. It appears that this correlation yields reasonably good prediction of k_s for the graphite surface (the over-estimation is about 8 %), and under-prediction in the case of the grid-blasted surface. The correlation of De Marchis *et al.* (2020) was developed by studying the flow over irregular roughness, obtained by superimposing sinusoidal functions with random amplitudes, and directly yields a

prediction for ΔU^+ as a function of S_a and ES. The equivalent sand-grain roughness height can then be obtained by enforcing universality of the roughness function to the fully rough asymptote. This correlation yields the best results for the grit-blasted surface (the error is about 10 %), and under-prediction in the case of the graphite surface. Last, Jouybari *et al.* (2021) used supervised machine learning to predict k_s from experimental and numerical database, using DNN and GPR. The trained DNN and GPR networks can be accessed online at https://github.com/MostafaAghaei/Prediction-of-the-roughness-equivalent-sandgrain-height. The rough surfaces have been uploaded and the networks have been used to make predictions of k_s. We found that GPR yields lower errors with respect to our DNS data than those obtained by the DNN method. Furthermore, the error is smaller for the graphite surface than for the grit-blasted case.

5. Conclusion

We have carried out DNS of flow through rough pipes for two types of rough surfaces, up to the fully rough regime, thus simulating for the first time via DNS pipes with realistic rough walls. Although the relative roughness is quite large ($k/R = 0.186, 0.199$), we find that Townsend's outer-layer similarity hypothesis is satisfied at the highest Reynolds numbers under consideration, with deviations from the smooth wall case of 4 % for the grit-blasted surface and 13 % for the graphite surface. Hence, the traditional approach for defining the equivalent sand-grain roughness based on the definition of a roughness function for the log layer works quite well. Despite general similarity, we find some differences with respect to the classical study of Nikuradse (1933). First, we find that the friction factor in the laminar region is higher by about 5–9 % than the theoretical value for Hagen–Poiseuille flow. This discrepancy is however absorbed if the hydraulic radius is used in the definition of the Reynolds number. Second, the critical Reynolds number at which transition from laminar to turbulent motion occurs is less than in Nikuradse's experiments, and dependent on the type of geometry. These results agree with the experimental findings of Huang *et al.* (2013), who noticed that this behaviour occurs for relative roughness $k/R \gtrsim 0.14$, which is less than the cases under scrutiny here.

According to the classical interpretation for sufficiently small roughness (Jiménez 2004), for a specific type of surface the roughness function should be a function of k^+ only, and should not depend on the relative roughness, nor on the geometry of the duct. This also implies that the trend of the roughness function should be the same for the pipes and the channels with the same rough surface. However, here we find differences of the roughness function of about 5 % with respect to the case of a plane channel (Busse *et al.* 2017). These are most likely due to the large relative roughness of the surfaces under consideration, which points to non-negligible effect of the duct geometry, yielding differences in the reduction coefficient.

The distributions of the velocity fluctuations also show differences from the smooth wall case. First, the peak of the streamwise velocity variance no longer shows clear increase with the Reynolds number, but rather depends on the shape of the roughness, with slight decline for the graphite surface, and slight increase for the grit-blasted surface. The peaks of the other two velocity components are instead higher than in the smooth wall case, as a consequence of isotropisation of turbulence as the rough surface is approached (Orlandi, Sassun & Leonardi 2016). Moreover, the position of the peaks lies within the roughness canopy as the Reynolds number increases, as the turbulence structures can penetrate deeper. We have finally found that existing correlations generally fail in predicting the equivalent sand-grain roughness height for the roughness types under consideration. Among all the considered correlations, the one developed by De Marchis *et al.* (2020)

	N_x	$N_y = N_z$	Δx^+	$\Delta y^+ = \Delta z^+$	Re_τ	$f \times 10^2$
		Grit-blasted surface Sensitivity to streamwise resolution at $Re_b = 4400$				
GB1	256	256	5.46	2.14	222.79	8.20
GB2	384	256	3.69	2.16	225.21	8.40
GB3	512	256	2.77	2.16	225.65	8.40
		Grit-blasted surface Sensitivity to cross-stream resolution at $Re_b = 4400$				
GB4	384	128	3.69	4.3	225.41	8.40
GB5	384	192	3.66	2.86	223.78	8.32
GB6	384	320	3.68	1.73	224.83	8.36
		Graphite surface Sensitivity to cross-stream resolution at $Re_b = 30\,000$				
GR7	1152	256	9.31	15.32	1709.78	10.36
GR8	1152	384	9.35	10.26	1716.65	10.48
GR9	1152	576	9.40	6.87	1726.40	10.56

Table 5. Results of the grid sensitivity study for grit-blasted surface at $Re_b = 4400$ and for graphite surface at $Re_b = 30\,000$.

yields the best prediction of k_s for the grit-blasted surface, whereas the correlation developed by Flack *et al.* (2020), which was intended for positively skewed rough surfaces, achieves the best results for the graphite surface. Despite significant errors in the prediction of k_s, it is worth noting that the roughness function should scale logarithmically with k_s^+. Hence, even in the presence of substantial errors in predicting k_s, the estimated equivalent sand-grain roughness values may still be satisfactory for drag prediction.

Follow-up studies should include DNS of surfaces with lower relative roughness, to satisfy the constraints set by Jiménez (2004). The resulting database could then be used to develop improved predictive correlations for the equivalent sand-grain roughness height.

Supplementary material. Computational Notebook files are available as supplementary material at https://doi.org/10.1017/jfm.2023.728 and online at https://www.cambridge.org/S0022112023007280/JFM-Notebooks.

Acknowledgements. We acknowledge that the results reported in this paper have been achieved using the PRACE Research Infrastructure resource GALILEO100 based at CINECA, Casalecchio di Reno, Italy. The authors would like to thank N. Sandham and coworkers for making available the roughness geometries. Many interesting conversations with P. Orlandi are also gratefully acknowledged.

Funding. This work received funding from AVIO SpA and from Regione Lazio in the form of the PhD scholarship of the leading author.

Declaration of interests. The authors report no conflict of interest.

Author ORCIDs.
Mariangela De Maio https://orcid.org/0000-0003-1516-1491;
Beatrice Latini https://orcid.org/0000-0002-7838-7212;
Francesco Nasuti https://orcid.org/0000-0003-2798-5869;
Sergio Pirozzoli https://orcid.org/0000-0002-7160-3023.

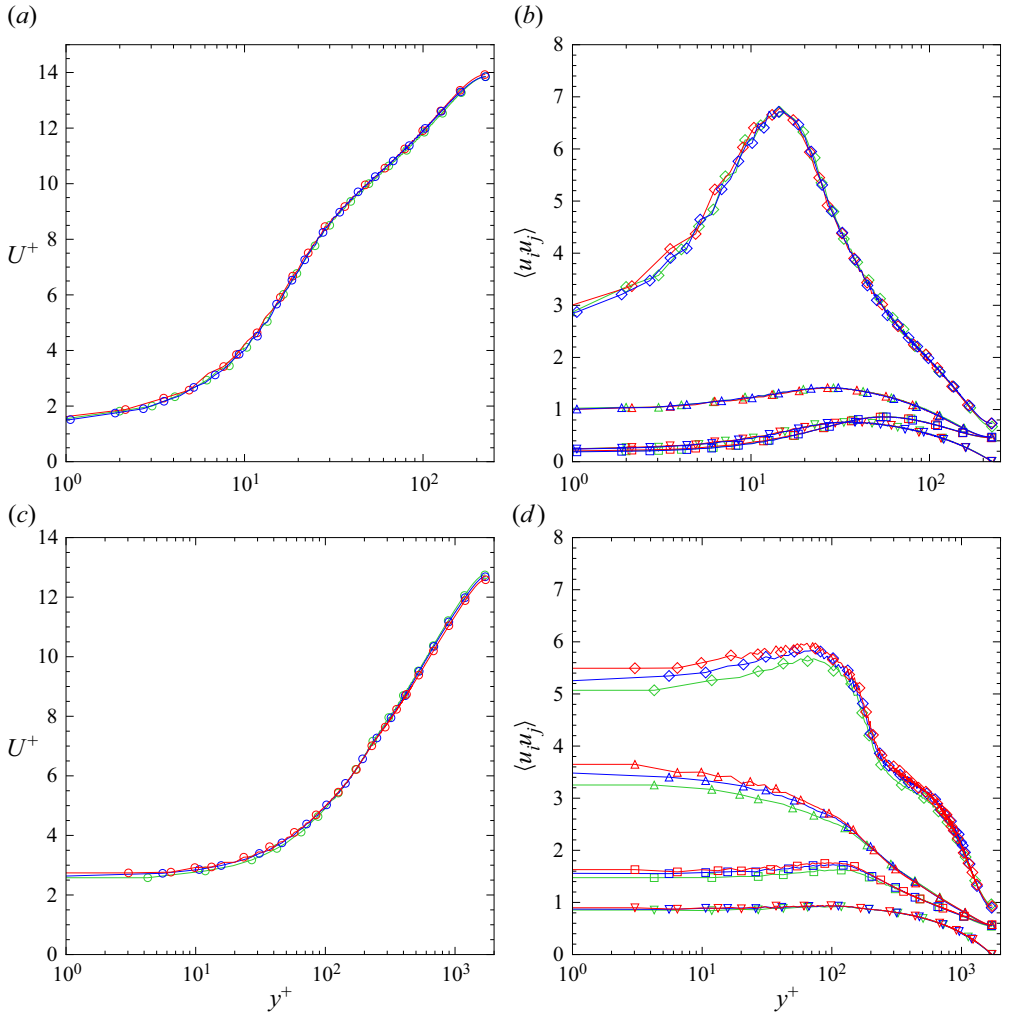

Figure 13. Grid sensitivity analysis for grit-blasted surface at $Re_b = 4400$ (*a*,*b*), and for graphite surface at $Re_b = 30\,000$ (*c*,*d*). The color codes denote different grids (see table 5 for reference). In panels (*a*,*b*): GB5 (red, selected for the analysis), GB3 (green), GB6 (blue). In panels (*c*,*d*): GR9 (red, selected for the analysis), GR7 (green), GR8 (blue). Symbols denote: U (○), $\langle u_x^2 \rangle$ (◇), $\langle u_r^2 \rangle$ (□), $\langle u_\Theta{}^2 \rangle$ (△) and $\langle u_x u_r \rangle$ (▽). The directory including the data and the Jupyter notebook can be accessed at https://www.cambridge.org/S0022112023007280/JFM-Notebook/files/Figure-13.

Appendix. Grid sensitivity analysis

In this appendix we report the results of a grid sensitivity analysis that we performed at $Re_b = 4400$ for the grit-blasted surface, and at $Re_b = 30\,000$ for the graphite surface. The key parameters for this study are reported in table 5, including number of grid points and friction coefficient. In the case of the grit-blasted surface, grid coarsening and refinement along the streamwise and cross-stream directions was tested, with respect to the baseline mesh (GB5). The percentage errors in the friction coefficient observed in the most refined grids (GB3 and GB6) in relation to the reference mesh (GB5) remained below 1 %. In the case of the graphite surface, grid coarsening along the cross-stream directions was considered with respect to the baseline mesh (GR9). Differences in the friction factor between the GR8 grid and the finest grid (GR9) are below 1 %.

A more detailed analysis of numerical uncertainties is offered in figure 13, where we compare the computed profiles of the mean velocity and of turbulent stresses. Whereas the mean velocity profiles show virtual collapse with respect to grid change, some effect of grid resolution is observed in the turbulent stresses (which we quantify in 4 %, at most), limited to the flow region near the crest of the roughness, which points to possible under-resolution of some small roughness element, whose effect on the overall flow is however negligible.

References

Bernardini, M., Modesti, D. & Pirozzoli, S. 2016 On the suitability of the immersed boundary method for the simulation of high-Reynolds-number separated turbulent flows. *Comput. Fluids* **130**, 84–93.

Burattini, P., Leonardi, S., Orlandi, P. & Antonia, R.A. 2008 Comparison between experiments and direct numerical simulations in a channel flow with roughness on one wall. *J. Fluid Mech.* **600**, 403–426.

Busse, A., Lützner, M. & Sandham, N.D. 2015 Direct numerical simulation of turbulent flow over a rough surface based on a surface scan. *Comput. Fluids* **116**, 129–147.

Busse, A. & Sandham, N.D. 2012 Parametric forcing approach to rough-wall turbulent channel flow. *J. Fluid Mech.* **712**, 169–202.

Busse, A., Thakkar, M. & Sandham, N.D. 2017 Reynolds-number dependence of the near-wall flow over irregular rough surfaces. *J. Fluid Mech.* **810**, 196–224.

Calignano, F., Manfredi, D., Ambrosio, E.P., Iuliano, L. & Fino, P. 2013 Influence of process parameters on surface roughness of aluminum parts produced by DMLS. *J. Adv. Manuf. Technol.* **67** (9), 2743–2751.

Chan, L., MacDonald, M., Chung, D., Hutchins, A.N. & Ooi, A. 2015 A systematic investigation of roughness height and wavelength in turbulent pipe flow in the transitionally rough regime. *J. Fluid Mech.* **771**, 743–777.

Chung, D., Hutchins, N., Schultz, M.P. & Flack, K.A. 2021 Predicting the drag of rough surfaces. *Annu. Rev. Fluid Mech.* **53**, 439–471.

Clauser, F.H. 1954 Turbulent boundary layers in adverse pressure gradients. *J. Aeronaut. Sci.* **21** (2), 91–108.

Colebrook, C.F., Blench, T., Chatley, H., Essex, E.H., Finniecome, J.R., Lacey, G., Williamson, J. & Macdonald, G.G. 1939 Correspondence. Turbulent flow in pipes, with particular reference to the transition region between the smooth and rough pipe laws (includes plates). *J. Inst. Civil Engrs* **12** (8), 393–422.

De Marchis, M., Napoli, E. & Armenio, V. 2010 Turbulence structures over irregular rough surfaces. *J. Turbul.* **11**, N3.

De Marchis, M., Saccone, D., Milici, B. & Napoli, E. 2020 Large eddy simulations of rough turbulent channel flows bounded by irregular roughness: advances toward a universal roughness correlation. *Flow Turbul. Combust.* **105** (2), 627–648.

Flack, K.A. & Schultz, M.P. 2010 Review of hydraulic roughness scales in the fully rough regime. *Trans. ASME J. Fluids Engng* **132** (4), 041203.

Flack, K.A. & Schultz, M.P. 2023 Hydraulic characterization of sandpaper roughness. *Exp. Fluids* **64** (1), 3.

Flack, K.A., Schultz, M.P. & Barros, J.M. 2020 Skin friction measurements of systematically-varied roughness: probing the role of roughness amplitude and skewness. *Flow Turbul. Combust.* **104** (2), 317–329.

Flack, K.A., Schultz, M.P., Barros, J.M. & Kim, Y.C. 2016 Skin-friction behavior in the transitionally-rough regime. *Intl J. Heat Fluid Flow* **61**, 21–30.

Flack, K.A., Schultz, M.P. & Rose, W.B. 2012 The onset of roughness effects in the transitionally rough regime. *Intl J. Heat Fluid Flow* **35**, 160–167.

Flack, K.A., Schultz, M.P. & Shapiro, T.A. 2005 Experimental support for Townsend's Reynolds number similarity hypothesis on rough walls. *Phys. Fluids* **17** (3), 035102.

Forooghi, P., Stroh, A., Magagnato, F., Jakirlić, S. & Frohnapfel, B. 2017 Toward a universal roughness correlation. *J. Fluids Engng* **139** (12), 121201.

Hama, F.R. 1954 Boundary layer characteristics for smooth and rough surfaces. *Trans. Soc. Nav. Archit. Mar. Engrs* **62**, 333–358.

Harlow, F. & Welch, J. 1965 Numerical calculation of time-dependent viscous incompressible flow of fluid with free surface. *Phys. Fluids* **8** (12), 2182.

HOYAS, S. & JIMENEZ, J. 2006 Scaling of the velocity fluctuations in turbulent channels up to $re_\tau = 2003$. *Phys. Fluids* **18** (1), 011702.

HUANG, K., WAN, J.W., CHEN, C.X., LI, Y.Q., MAO, D.F. & ZHANG, M.Y. 2013 Experimental investigation on friction factor in pipes with large roughness. *Exp. Therm. Fluid Sci.* **50**, 147–153.

IACCARINO, G. & VERZICCO, R. 2003 Immersed boundary technique for turbulent flow simulations. *Appl. Mech. Rev.* **56** (3), 331–347.

JELLY, T.O., RAMANI, A., NUGROHO, B., HUTCHINS, N. & BUSSE, A. 2022 Impact of spanwise effective slope upon rough-wall turbulent channel flow. *J. Fluid Mech.* **951**, A1.

JIMÉNEZ, J. 2004 Turbulent flows over rough walls. *Annu. Rev. Fluid Mech.* **36**, 173–196.

JOUYBARI, M.A., YUAN, J., BRERETON, G.J. & MURILLO, M.S. 2021 Data-driven prediction of the equivalent sand-grain height in rough-wall turbulent flows. *J. Fluid Mech.* **912**, A8.

KANDLIKAR, S.G., SCHMITT, D., CARRANO, A.L. & TAYLOR, J.B. 2005 Characterization of surface roughness effects on pressure drop in single-phase flow in minichannels. *Phys. Fluids* **17** (10), 100606.

KIM, J. & MOIN, P. 1985 Application of a fractional-step method to incompressible Navier–Stokes equations. *J. Comput. Phys.* **59**, 308–323.

LEONARDI, S., ORLANDI, P., DJENIDI, L. & ANTONIA, R.A. 2004 Structure of turbulent channel flow with square bars on one wall. *Intl J. Heat Fluid Flow* **25** (3), 384–392.

LUMLEY, J.L. 1979 Computational modeling of turbulent flows. *Adv. Appl. Mech.* **18**, 123–176.

MACDONALD, M., HUTCHINS, N. & CHUNG, D. 2019 Roughness effects in turbulent forced convection. *J. Fluid Mech.* **861**, 138–162.

MARUSIC, I., BAARS, W.J. & HUTCHINS, N. 2017 Scaling of the streamwise turbulence intensity in the context of inner-outer interactions in wall turbulence. *Phys. Rev. Fluids* **2**, 100502.

NASUTI, F., TORRICELLI, A. & PIROZZOLI, S. 2021 Conjugate heat transfer analysis of rectangular cooling channels using modeled and direct numerical simulation of turbulence. *Intl J. Heat Mass Transfer* **181**, 121849.

NIKITIN, N. & YAKHOT, A. 2005 Direct numerical simulation of turbulent flow in elliptical ducts. *J. Fluid Mech.* **532**, 141–164.

NIKURADSE, J. 1926 *Untersuchung über die Geschwindigkeitsverteilung in turbulenten Strömungen*. VDI-Verlag.

NIKURADSE, J. 1933 *Strömungsgesetze in rauhen rohren*. VDI-Forsch.

ORLANDI, P. 2000 *Fluid Flow Phenomena: A Numerical Toolkit*, vol. 55. Springer.

ORLANDI, P. & LEONARDI, S. 2006 DNS of turbulent channel flows with two- and three-dimensional roughness. *J. Turbul.* **7**, N73.

ORLANDI, P., LEONARDI, S. & ANTONIA, R.A. 2006 Turbulent channel flow with either transverse or longitudinal roughness elements on one wall. *J. Fluid Mech.* **561**, 279–305.

ORLANDI, P., MODESTI, D. & PIROZZOLI, S. 2018 DNS of turbulent flows in ducts with complex shape. *Flow Turbul. Combust.* **100** (4), 1063–1079.

ORLANDI, P., SASSUN, D. & LEONARDI, S. 2016 DNS of conjugate heat transfer in presence of rough surfaces. *Intl J. Heat Mass Transfer* **100**, 250–266.

O'ROURKE, J., *et al.* 1998 *Computational Geometry in C*. Cambridge University Press.

PIROZZOLI, S., BERNARDINI, M. & ORLANDI, P. 2016 Passive scalars in turbulent channel flow at high Reynolds number. *J. Fluid Mech.* **788**, 614–639.

PIROZZOLI, S., MODESTI, D., ORLANDI, P. & GRASSO, F. 2018 Turbulence and secondary motions in square duct flow. *J. Fluid Mech.* **840**, 631–655.

PIROZZOLI, S., ROMERO, J., FATICA, M., VERZICCO, R. & ORLANDI, P. 2021 One-point statistics for turbulent pipe flow up to $Re_\tau \approx 6000$. *J. Fluid Mech.* **926**, A28.

POPE, S.B. 2000 *Turbulent Flows*. Cambridge University Press.

SCHLICHTING, H. 1936 Experimentelle untersuchungen zum rauhigkeitsproblem. *Ing.-Arch.* **7** (1), 1–34.

SCHULTZ, M.P. & FLACK, K.A. 2007 The rough-wall turbulent boundary layer from the hydraulically smooth to the fully rough regime. *J. Fluid Mech.* **580**, 381–405.

SNYDER, J.C., STIMPSON, C.K., THOLE, K.A. & MONGILLO, D. 2016 Build direction effects on additively manufactured channels. *J. Turbomach.* **138** (5), 051006.

STIMPSON, C.K., SNYDER, J.C., THOLE, K.A. & MONGILLO, D. 2016 Roughness effects on flow and heat transfer for additively manufactured channels. *J. Turbomach.* **138** (5), 051008.

THAKKAR, M. 2017 *Investigation of turbulent flow over irregular rough surfaces using direct numerical simulations*. PhD thesis, University of Southampton.

THAKKAR, M., BUSSE, A. & SANDHAM, N. 2016 Dataset for surface correlations of hydrodynamic drag for transitionally rough engineering surfaces. https://eprints.soton.ac.uk/392562/.

THAKKAR, M., BUSSE, A. & SANDHAM, N. 2017 Surface correlations of hydrodynamic drag for transitionally rough engineering surfaces. *J. Turbul.* **18** (2), 138–169.

THAKKAR, M., BUSSE, A. & SANDHAM, N.D. 2018 Direct numerical simulation of turbulent channel flow over a surrogate for Nikuradse-type roughness. *J. Fluid Mech.* **837**, R1.

TOWNSEND, A.A.R. 1976 *The Structure of Turbulent Shear Flow*. Cambridge University Press.